International Journal of Material Forming (2026) 19:15
https://doi.org/10.1007/s12289-026-01985-0

RESEARCH

Numerical simulation of material flow in AA7075 during constrained friction processing

George Diyoke[1] · Camila C. de Castro[2] · Rupesh Chafle[1] · Benjamin Klusemann[1,2]

Received: 4 December 2025 / Accepted: 27 January 2026

Abstract

Lightweight aluminum alloys, such as AA7075, are desirable for applications in various industries, but their limited formability and workability often pose significant challenges. Constrained Friction Processing (CFP) has emerged as a promising technique to address these challenges by refining microstructures through the relative motion between two tools and the workpiece. The process involves axial extrusion, dual tool rotation, and constraint of the extrudate to control material flow and enhance microstructural refinement. CFP is particularly attractive for high-strength AA7075 as it imposes constrained material flow and increased shear deformation, overcoming the limited formability observed in existing conventional extrusion processes. This study investigates CFP using both experimental and numerical methods, establishing correlations between process conditions, material flow, microstructural evolution, and hardness for the aluminum alloy AA7075. The process was investigated at rotational speeds of 1000–1400 rpm, resulting in the highest measured peak temperature up to 445°C and refined grain sizes of 2–3 µm. The results show that initial shear deformation and material flow under the rotating tools are redistributed during processing, leading to helical flow behavior in the extruded rod. The refined stir zone (SZ) exhibited increase in hardness, about 25% compared to the base material. The developed finite-element model demonstrates good agreement with experimental results with respect to the complete thermal cycle, spatial temperature distribution, and material flow patterns, providing insight into the microstructural evolution during CFP of aluminium alloys.

Keywords Process simulation · Constrained friction processing (CFP) · Material flow behavior · Dynamic recrystallization · Microstructural zones

Introduction

The use of aluminum alloys has gained significant attention due to their advantageous combination of low density and excellent mechanical properties, including high strength, fatigue resistance, and ductility [1, 2]. These attributes have led to an increasing demand for aluminum alloys across various industries, such as electronics, aerospace, and automotive [3, 4]. Among these alloys, AA7075 has emerged as a material of interest due to its superior mechanical properties, which are achieved primarily through precipitation-strengthening mechanisms. The alloying elements such as Zn, Mg, and Cu play a critical role in this strengthening process [5, 6]. An increased content of Zn, Mg, and Cu, as well as a higher Zn/Mg ratio in Al–Zn–Mg–Cu alloys, such as AA7075, has proven to be an effective strategy for promoting the formation of dispersive nano-sized precipitates, such as η' and η phases [7, 8]. Despite the strength benefits

✉ George Diyoke
george.diyoke@hereon.de

Camila C. de Castro
camila.castro@leuphana.de

Rupesh Chafle
rupesh.chafle@hereon.de

Benjamin Klusemann
benjamin.klusemann@hereon.de

[1] Institute of Material and Process Design, Helmholtz-Zentrum Hereon, Max-Planck-Straße 1, Geesthacht 21502, Germany

[2] Institute for Production Technology and Systems, Leuphana University Lüneburg, Universitätsallee 1, Lüneburg 21335, Germany

Published online: 11 February 2026

of alloy-rich compositions, they significantly deteriorate formability and workability [6, 9, 10], thereby limiting their applicability.

To address this challenge, severe plastic deformation (SPD) is often employed at elevated forming temperatures to enhance ductility and improve workability [5]. These techniques operate below the melting point, thus avoiding undesirable metallurgical reactions such as porosity or alloy segregation. Conventional solid-state processing methods, such as hot extrusion [11], rolling [12], and equal channel angular pressing (ECAP) [13], have been successfully applied to process AA7075, yielding significant grain refinement. Constrained friction processing (CFP) is a new solid-state processing technique [14], developed to process lightweight materials, with initial applications focused in Mg alloys, to achieve rods with fine-grained microstructures. The process is a variant of the refill friction stir spot welding (refill FSSW) process developed and patented at the Helmholtz-Zentrum Hereon, Germany [15]. The mechanism of CFP involves relative rotation of the shoulder and probe against a stationary workpiece held by a clamping ring, as illustrated in Fig. 1(a). The process takes place as follows: the rotating shoulder plunges downward into the fixed workpiece, causing extrusion, while the upward-moving probe rotates on the extruded rod. The rotation and upward movement of the probe on the rod, as shown in Fig. 1(b), constrains the flow of the material in contrast to free extrusion of the material in the absence of a probe, see Fig. 1(c). The latter process would be similar to friction extrusion (FE), where extrusion occurs by relative rotation of a single tool with respect to the workpiece, allowing a free flow of the extruded rod through the tool internal cavity [16]. While both processes produce rod-like products, CFP enables enhanced deformation under constrained conditions with the presence of the probe distinguishing it from the FE process. However, the presence of this additional tool part also leads to the main limitation of the process, which is the maximum length of the processed rod limited by the maximum displacement of the tool parts set to 20 mm for the equipment currently available.

In many friction-based solid-state processing techniques, the major challenge lies in understanding the interplay between process conditions and the resulting deformation mechanisms. In this context, process parameters such as rotational speed are important, as they influence grain refinement and microstructural evolution during processing. The CFP process has demonstrated the ability to reduce grain size from 1 mm in the as-cast state to 4 µm in Mg-Zn-Ca alloy, significantly enhancing both the compressive yield strength and ultimate strength [17]. Similarly, during the processing of the AM50 Mg alloy, the secondary phases were refined, with the average size of the intermetallic particles reduced from several micrometers to approximately 560 nm [18]. These experimental studies highlight the importance of rotational speed in driving localized heat generation and plastic deformation, which drives the material flow.

Understanding the material flow is crucial for optimizing process parameters. Computational models offer insights into flow behavior which complements experimental results. Zhang et al. [19] developed a computational fluid dynamics (CFD) model for FE of AA6061 to investigate material flow during processing. In this model, the material is assumed to behave as a non-Newtonian fluid. Their simulations revealed a helical flow pattern, providing initial insights into the complex flow dynamics. Lei et al. [20] investigated the flow behavior in FE using a smoothed particle hydrodynamics (SPH) model to simulate the extrusion of tubes. Their findings confirmed the helical material flow during extrusion. Similarly, Baffari et al. [21], in their 3D finite element method (FEM) simulation of the FE process, studied the material flow during the extrusion of magnesium alloy chips. Their results demonstrated a helical flow pattern in the extrudate through point tracking and flow analysis.

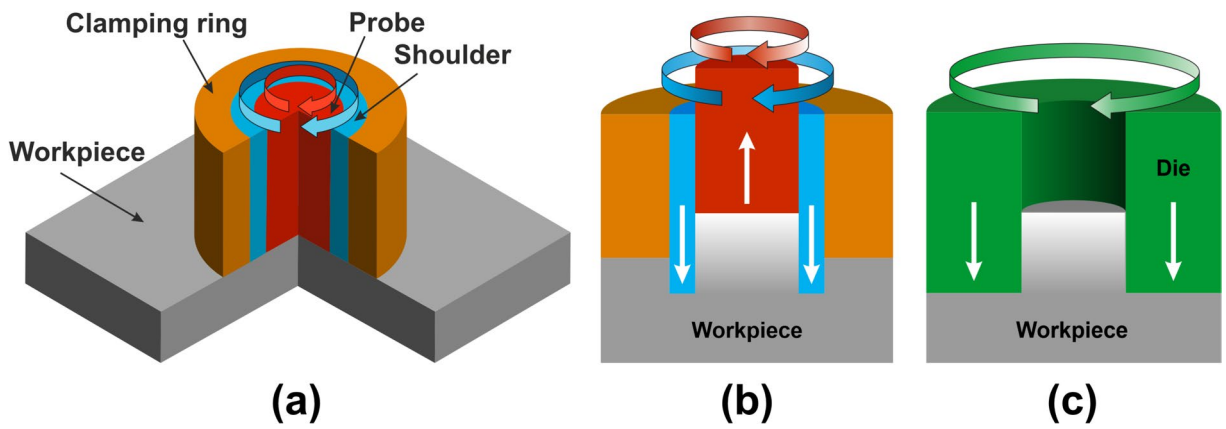

Fig. 1 Process assembly during friction-based extrusion: (**a**) CFP setup, (**b**) CFP process, and (**c**) FE process comparable to CFP without a probe

Table 1 Chemical composition of AA7075 aluminum alloy (wt.%) [22]

Element	Zn	Mg	Cu	Cr	Fe	Si	Mn	Al
Wt.%	5.6–6.1	2.1–2.6	1.2–1.6	0.18–0.28	≤0.50	≤0.40	≤0.30	Balance

Table 2 Mechanical properties of as-rolled AA7075-T7351 aluminum [22]

Property	Value
Yield strength, $\sigma_{0.2}$ (MPa)	240–280
Ultimate tensile strength (MPa)	360–410
Elongation to failure (%)	8–12
Vickers hardness (HV)	140–155

Table 3 Employed process parameters: rotational speed, plunge speed, and clamping force

Rotational speed	Plunge speed	Clamping force
1000 rpm		
1200 rpm	1.0 mm s^{-1}	12 kN
1400 rpm		

All the above studies provide an understanding of material flow in FE, which shares some characteristic similarities but also distinct differences with CFP, which remains underexplored.

To address this, the work presents a numerical model that investigates material flow in the CFP process, focusing on shear-induced deformation and the formation of helical flow features. The simulation also explores the influence of varying process conditions, such as the absence of the probe and rotation as well as different rotational speeds on material flow and microstructure evolution, which are compared to experimental results.

Materials and methods

In the experiments, sheets of AA7075-T7351 are used as base material (BM) and cut into workpieces of 25×25×6.2 mm³. Owing to the rolling process, the grains were elongated rather than equiaxed. The BM grain size was therefore characterized in two dimensions, yielding an average grain length of 177 µm along the rolling direction and an average grain width of 15.6 µm in the transverse direction. Other material descriptions such as the chemical composition and mechanical properties of the alloy are listed in Tables 1 and 2 respectively. The CFP is performed using the RPS200 (Harms & Wende, Germany) refill FSSW system operated using position control. The tool setup consisted of a ∅17 mm clamping ring, a ∅9 mm shoulder and a ∅6 mm probe, all made of H13 tool steel. During the processing, the shoulder and probe's relative speed are kept at 1.00 : 1.25 to account for volume conservation in relation to the displaced volume of material and the shoulder's cavity volume.

In order to evaluate the influence of rotational speeds on the temperature evolution during the CFP, extrudates are produced using the parameters presented in Table 3. The measurements are done using ∅0.5 mm K-type thermocouples,[1] placed in the base material at the positions T1 and T2 as depicted in Fig. 2(a). The in-process temperature evolution are acquired using a signal acquisition system coupled with LabView engineering software at a frequency of 50 Hz. An acquisition frequency of 50 Hz is selected as it provides a good balance between the necessary resolution of the measurements and computational resource requirements during data acquisition, as reported in previous works [18]. Furthermore, the CFP process is modified to operate without the probe in the assembly to mimic the FE process (see Fig. 1(c)).

The visualization of the material flow is achieved by the addition of tracer material (TM) to the base material before processing. Pieces of pure copper wire with a diameter of ∅1.5 mm are positioned in the sheet according to the schematic depicted in Fig. 2(b). The cross-section observed are precisely obtained through progressive grinding of the extrudate, as shown in Fig. 2(c).

The microstructure and material flow of the processed extrudates are analyzed using a VHX-6000 digital microscope (Keyence, Germany) with polarized light. For that purpose, the samples are prepared according to standard metallographic preparation: cutting and embedding of the specimens, followed by grinding and polishing using 1.0 μm diamond suspension. For the microstructural analysis, the polished samples are electrolytically etched for 120 s at 15 V using Barker's solution.

Micrographs for the determination of grain sizes were acquired using the Leica DMi8 inverted microscope (Leica Microsystems, Germany) with polarized light. The measurements of both the base material and the processed samples were determined using the intercept method, based on the average values along horizontal and vertical lines. Hardness measurements are performed on the polished surfaces of naturally-aged processed samples, the Durascan 70 G5 (EMCO-TEST Prüfmaschinen GmbH, Austria) equipped with a micro-Vickers indenter, using a load of 100 g and a distance of 0.15 mm between each indentation.

[1] The precision of the measurements is calculated according to the thermocouple, defined as ±2.2 °C for $T < 293.3$ °C and ±0.0075% T for $T \geq 293.3$ °C.

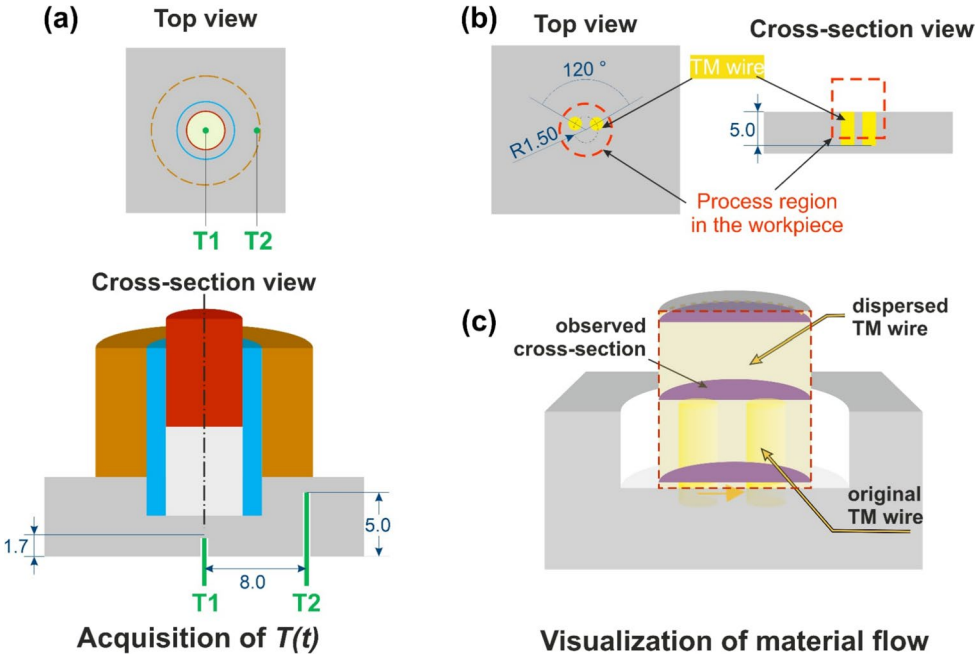

Fig. 2 Schematic of temperature acquisition during CFP and visualization of the material flow: (**a**) thermocouple (TC) location at T1 and T2 in the workpiece for the temperature acquisition during the process, (**b**) position of the tracer material (TM) wires on the workpiece to be processed, and (**c**) cross-sections for the observation of the material flow. All dimensions in mm

Process model

Figure 3 illustrates the tool parts and workpiece used to model CFP in the Deform®3D environment, with dimensions and the mesh domain of the workpiece. Figure 3(a) depicts the clamping ring, which holds the workpiece by exerting pressure uniformly around the circumference and represents the reference for the alignment of other CFP components in the assembly. Figure 3(b) shows the shoulder, which fits into the clamping ring. Fig. 3(c), depicts a non-hollow cylinder modeled as the probe, positioned inside the hollow shoulder during the process. The clamping ring, shoulder, and probe are assumed as rigid bodies, meshed with 10,000 tetrahedral elements to account for heat transfer, based on H13 tool steel material properties as provided in Table 4. Figure 3(d) illustrates the workpiece, which is discretized via 80,000 tetrahedral elements. The variable element size aids in re-meshing and forms a dense mesh at the center of the workpiece, which is in contact with the shoulder and the probe. The re-meshing step parameter of 0.7 corresponds to the interference depth used to trigger automatic re-meshing. At the contact region, the re-meshing ensures a higher quality of the mesh by

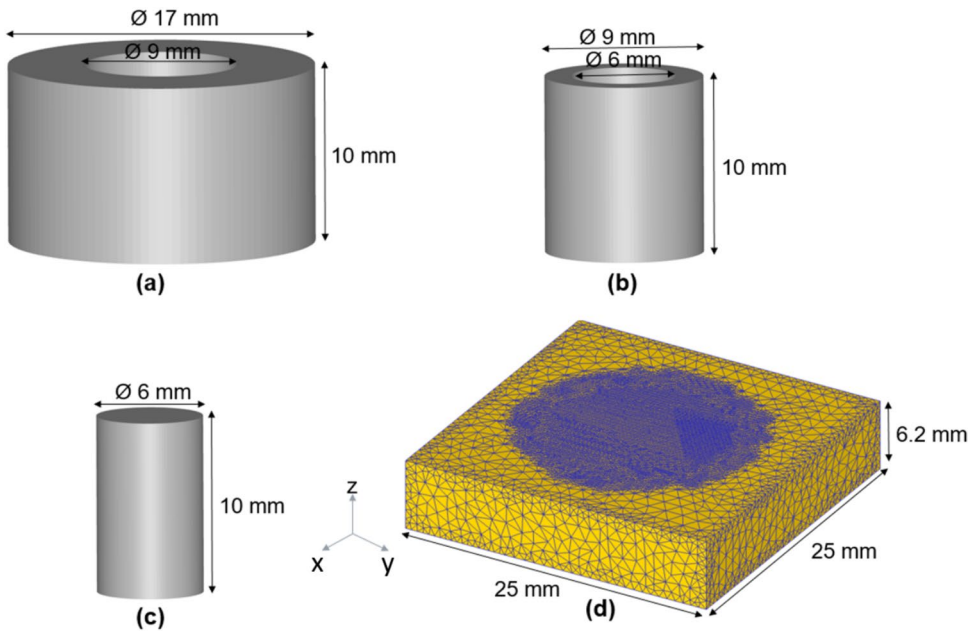

Fig. 3 Schematic tools and workpiece used in CFP modeling; (**a**) clamping ring (**b**) shoulder, (**c**) probe, and (**d**) workpiece showing the mesh density. The coordinate system also represents x: radial direction (RD), y: transverse direction (TD), and z: plunge direction (PD)

Table 4 Material parameters for AA7075, H13 tool steel and other simulation parameters employed in the CFP simulations

AA7075 workpiece parameters	Symbols	Magnitude	Units
Material constant	A	1.0×10^{9} [29, 30]	s^{-1}
Material constant	n	5.4 [29, 30]	-
Stress exponent	α	0.014 [29, 30]	MPa^{-1}
Activation energy	ΔH	129 [29, 30]	kJ mol^{-1}
Poissons ratio of Al	ν^{Al}	0.33	-
Density of Al	ρ^{Al}	2.67×10^{-6}	kg mm^{-3}
Thermal conductivity of Al	κ^{Al}	125	N s^{-1} $°C^{-1}$
Heat convection coefficient	$h^{convection}$	0.02	N s^{-1} mm^{-1} $°C^{-1}$
Heat conduction coefficient	$h^{conduction}$	11	N s^{-1} mm^{-1} $°C^{-1}$
Reference temperature of Al	T^{room}	20	°C
Taylor-Quinny factor	η	0.9 [31]	-
Shear friction factor	m	1.0 [28]	-
H13 tool steel parameters			
Poissons ratio of Steel	ν^{Steel}	0.3	-
Thermal conductivity of Steel	κ^{Steel}	245	N s^{-1} $°C^{-1}$
Reference temperature of Steel	T^{room}	20	°C
Other process parameters			
Shoulder axial speed	s^{speed}	1.0	mm s^{-1}
Probe axial speed	p^{speed}	1.25	mm s^{-1}
Shoulder and probe rotational speed	$RS^{sh.} = RS^{probe}$	1000, 1200, 1400	rpm
Simulation time step size	t^{step}	0.01	-
Total process time	$t^{process}$	3	s

conserving the thermo-mechanical state of the workpiece during the simulation [4]. The refined mesh density follows the shoulder movement, and the size is about 100 times smaller than the largest element size in the workpiece.

The mechanical boundary conditions applied to the rigid objects allow for specified movements, as illustrated in Fig. 1(a). The displacement degrees of freedom of the side and bottom faces of the workpiece are set to zero, preventing also any rigid body motions. The initial temperatures for the workpiece, shoulder, clamping ring, and probe are set to room temperature, i.e., 20°C. Additional thermal boundary conditions are imposed to define the thermal interactions between the various components and the environment. The primary heat transfer mechanism at contact region between the clamping ring, probe, shoulder, and the workpiece is conduction. Heat exchange between the workpiece, clamping ring, and the environment was modeled through convection to ambient air at room temperature and radiation, with parameters given in Table 4.

Material model, heat generation, and friction conditions

The workpiece material used is AA7075, which is modelled as rigid visco-plastic. The flow stress is predicted using a hyperbolic-sine constitutive equation that relies on an Arrhenius-type relationship expressed as

$$\dot{\bar{\varepsilon}} = A\left[\sinh(\alpha\bar{\sigma})\right]^{n}\exp\left(-\frac{\Delta H}{RT}\right), \tag{1}$$

where $\dot{\bar{\varepsilon}}$ is the strain rate, $\bar{\sigma}$ is the flow stress, ΔH is the activation energy, R is the universal gas constant, T is the absolute temperature, and A, n and α are material constants [23, 24]. The heat contribution due to friction and plastic deformation, at the workpiece-tool interface in CFP is simplified as $\dot{q} = \dot{q}_f + \dot{q}_p$, where $\dot{q}$ is the rate of total heat generated during the process, $\dot{q}_f$ is the rate of frictional heat generated, and $\dot{q}_p$ is the rate of heat generated due to plastic deformation of the material. The rate of frictional heating $\dot{q}_f$ is further expressed as $\dot{q}_f = \tau_f|v_s|$, where τ_f is the frictional shear force and v_s is the velocity at the interface of the workpiece and tool [25, 26]. In Deform®3D, the expression of heat generation due to plastic deformation, which incorporates the inelastic heat fraction, reads [27] $\dot{q}_p = \eta\bar{\sigma}\dot{\bar{\varepsilon}}$ where η is the inelastic heat fraction (Taylor-Quinny factor) or amount of mechanical work converted to heat. Although the Taylor–Quinney factor may vary with strain and temperature, a constant value of η = 0.9 is selected, which is consistent with prior FEM studies on aluminum alloys undergoing severe plastic deformation, where most plastic work is converted into heat.

To capture the mechanical interaction between rotating tools and the workpiece, the shear friction model is adopted. The expression for sticking condition in terms of friction factors is denoted as $\tau_{contact} = m\tau_{yield}$, where τ_{yield} is directly related to the shear yield strength of the material in sticking condition, and m is the friction factor. A shear friction factor of m = 1.0 is adopted to represents the sticking conditions at the tool–workpiece interface, which is commonly assumed in process simulations of extrusion [28].

Process simulation input parameters

Flow stress data of AA7075 alloy is deduced from literature results of hot compression tests conducted at deformation temperatures between 300 °C and 500 °C under strain rates

of 0.001-10 s^{-1} [29, 30]. The values used in the simulation are provided in Table 4. The shoulder plunges downwards at a constant speed s^{speed}, while the probe moves upwards at a constant higher speed $p^{\text{speed}} = 1.25s^{\text{speed}}$ to account for plastic incompressibility. The *RS* of the shoulder and the probe are same i.e. $RS^{\text{sh.}} = RS^{\text{probe}}$ with respective inputs as stated in Table 4. Other values used in the simulation setup to relate different thermal interactions between objects for convection and conduction are mentioned in Table 4.

To simulate severe bulk deformation such as CFP using Deform®3D, an implicit solver with a conjugate gradient iterative approach is employed, to achieve stable solutions under extreme deformation conditions. Typically, dynamic re-meshing increases the total number of elements after each re-meshing step if substantial mesh distortion are detected. Dynamic re-meshing inevitably introduces interpolation errors through excessive remeshing. In this study, this effect is controlled via the set interference depth, which limits severe mesh distortion and regulates frequent/excessive remeshing procedure, particularly at the tool–workpiece interface, thereby minimizing numerical errors while maintaining solution stability.

Results and discussion

Process thermal history

Figure 4 shows the thermal cycles measured at the two thermocouple locations T1 and T2 for different tool rotational speeds. At both locations, the heating phase is characterized by a progressive temperature rise due to frictional heating and plastic deformation, followed by a cooling phase as heat dissipates into the material's surrounding environment. In Fig. 4(a), the thermal cycle is shown at location T1, which is positioned near the process region where heat generation is highest. The peak temperature increases with tool rotational speed, reaching approximately 400°C at 1000 rpm, 420°C at 1200 rpm, and 445°C at 1400 rpm where experiment and simulation are in good agreement. A significant deviation between experiment and simulation is observed at 1000 rpm during the plunging phase, which may be attributed to a slight movement of the thermocouple during the process. Nevertheless, the simulation results reproduce the overall trends and show good agreement with the experimental data, particularly at higher rotational speeds, during both heating and cooling phases.

Figure 4(b) shows that the temperature rise at T2 is significantly less pronounced compared to T1, due to the proximity of the latter within the process region. The trends in both heating and cooling phases at T2 are consistent across all rotational speeds, with a maximum recorded temperature lower than that at T1 due to the larger distance to the plasticized region. The simulation results closely follow the experimental data, indicating that heat conduction away from the process region to the surrounding regions of the workpiece is well captured by the model. The contribution of the friction condition to deformation will be discussed next.

Material deformation and axial force

To gain insight into the mechanisms governing material flow at the onset of the process, the strain profile and tangential velocity fields are analyzed. Figure 5(a) illustrates the strain profile at a point in the workpiece under the shoulder where major deformation occurs during the process. At the onset of the process, the strain increases rapidly due to intense shearing under sticking friction conditions. Following this initial increase, the strain shows nearly a plateau until 0.5 s, after which it accumulates continuously at a slower rate. Based on these observations, three distinct stages can be

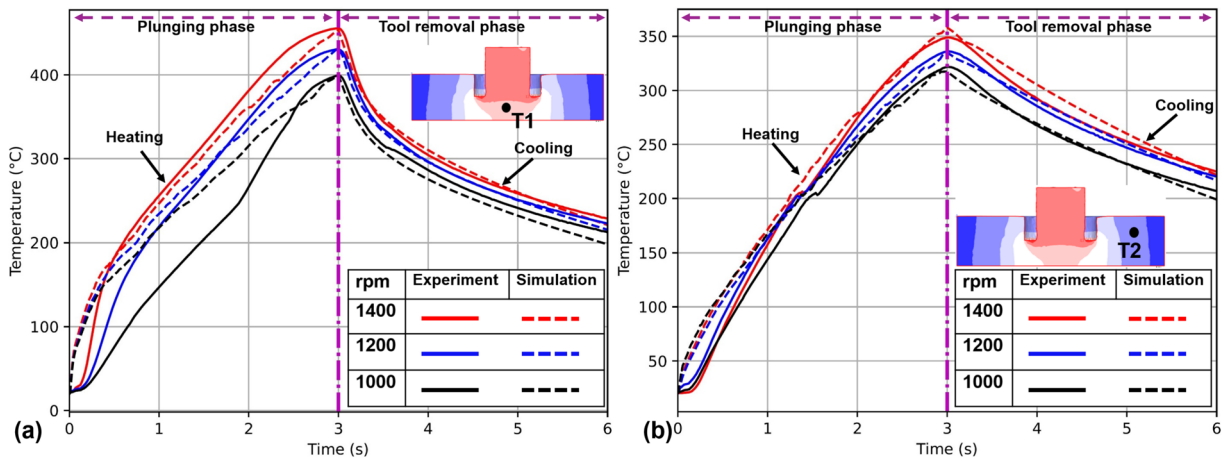

Fig. 4 Process thermal cycle on the workpiece at 1000, 1200, and 1400 rpm at two thermocouple positions: (**a**) T1 and (**b**) T2

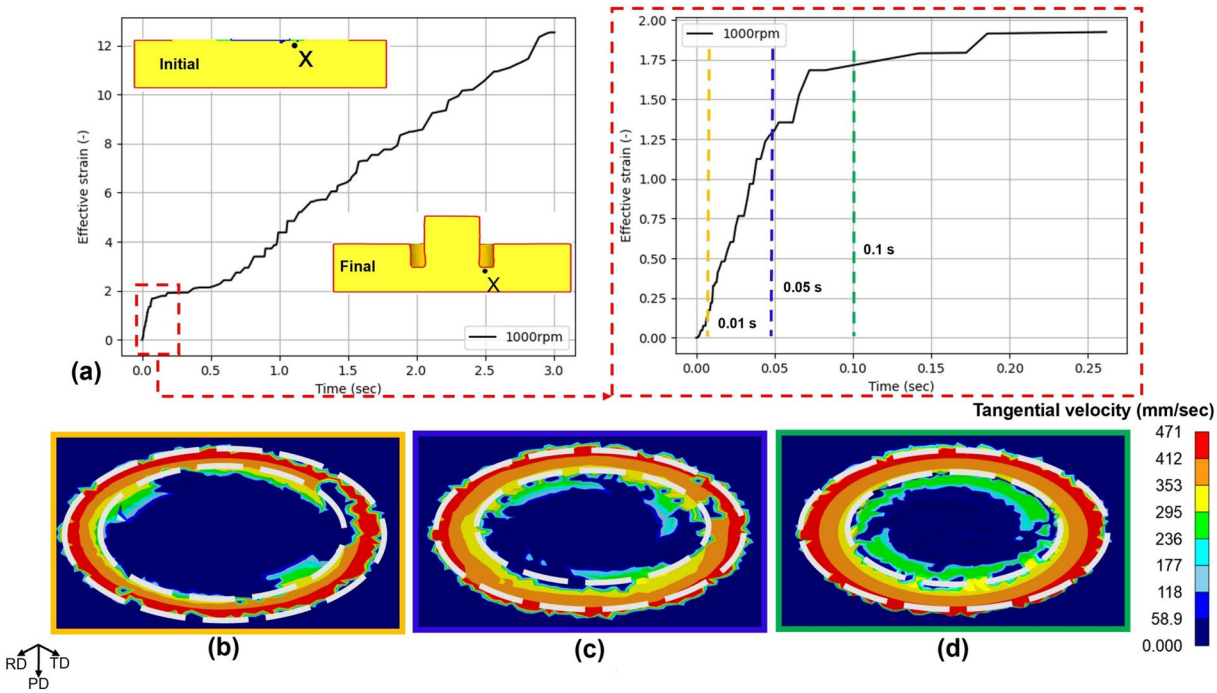

Fig. 5 Evolution of the workpiece deformation on the top plane: (**a**) showing initial and final positions of point X tracked under the shoulder to deduce the strain profile with initial rapid increase, and tangential velocity distribution at (**b**) $t^{process} = 0.01$ s, (**c**) $t^{process} = 0.05$ s, and (**d**) $t^{process} = 0.1$ s. The outer dashed circle represents the shoulder region, while the inner dashed circle indicates the probe region

defined at the workpiece surface before the tool penetrates extensively the workpiece: the initial stage at $t^{\text{stage}} = 0.01$ s, the transition stage at $t^{\text{stage}} = 0.05$ s, and the quasi-steady stage at $t^{\text{stage}} = 0.1$ s.

Figure 5(b-d) illustrates the evolution of tangential flow velocity at these stages on the top surface of the workpiece. At the initial stage of the process, at $t^{\text{stage}} = 0.01$ s, in Fig. 5(b), the tangential flow velocity in both the shoulder and probe regions captures the material deformation that results in flow of the workpiece with respect to the tool rotation. Under sticking friction conditions, the tangential velocity of the workpiece surface matches that of the tool. The tangential velocity is calculated as $v = \omega^{\text{sh.}} r$, where $\omega^{sh.}$ is the angular speed of the shoulder (or probe, ω^{probe}), and r is the radius of the tool. For instance, at 1000 rpm, initial shearing is observed at the circumference of the shoulder region (at r= 4.5 mm), with a maximum tangential velocity of 471 mm s^{-1}. Similarly, initial shearing is observed at the circumference of the probe region (at r = 3.0 mm), characterized by a tangential velocity of 314 mm s^{-1}. The strain profile reveals the initial transition and quasi-steady stages at the workpiece surface, with the corresponding tangential velocity distributions shown in Fig. 5(c) and (d). Beyond 0.1 s, the shoulder significantly penetrates the workpiece leading to extrusion. It is noted that the strain values reported here represent cumulative strain rather than critical strain for the onset of dynamic recrystallization (DRX). For aluminum alloys such as AA7075, DRX initiation typically occurs at much lower strains, generally in the range of 0.5–1 under appropriate temperature and strain-rate conditions [32]. Therefore, the high strain levels observed in the present simulations indicate sustained plastic deformation well beyond DRX initiation.

Figure 6(a–b) illustrates the shoulder and probe force profiles at different rotational speeds. The shoulder force increases rapidly at the initial stage due to the workpiece's resistance to deformation under the shoulder. On the other hand, the probe force decreases sharply at the initial stage due to reduced resistance to deformation. This also implies that the force exerted by the shoulder induces significant deformation on the workpiece compared to the force exerted by the probe. Furthermore, as rotational speed increases, the initial peak shoulder forces decrease, as shown in Fig. 6(a). This suggests that higher rotational speeds increase heat generation, leading to more softening of the material. After the initial peak, a rapid decrease in force for both shoulder and probe are observed because of increasing temperature leading to material softening. The shoulder force remains significantly higher than the probe force until the end of the process. During processing, distinct microstructural zones are formed in the workpiece due to the thermo-mechanical processing conditions, which will be discussed in the following.

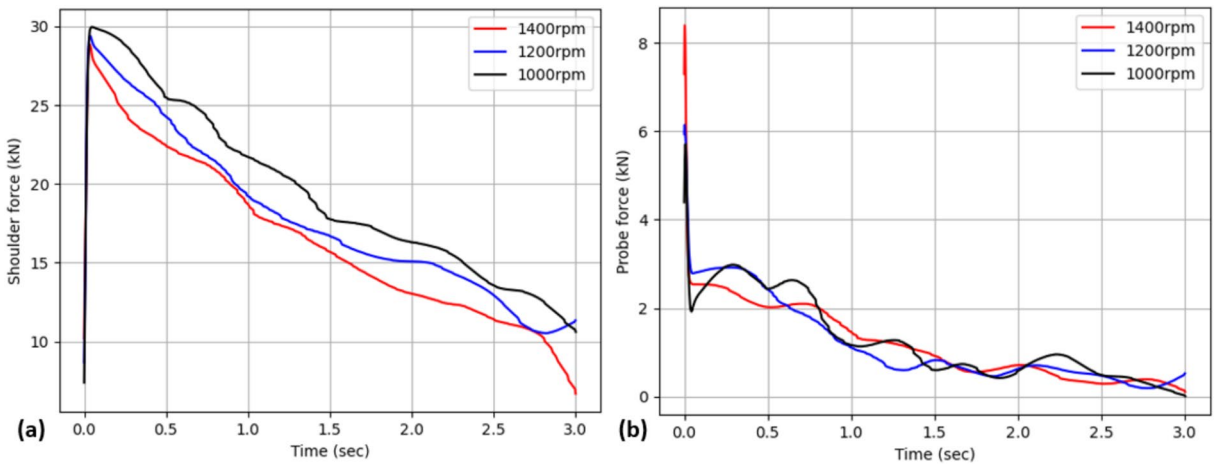

Fig. 6 Prediction of process force evolution during CFP at different rotational speeds for (**a**) the shoulder, and (**b**) the probe

Experimental characterization of the microstructural zones and hardness in the workpiece

The study aims to identify and characterize the distinct microstructural zones based on their microstructural features, such as morphology and grain size. As depicted in Fig. 7, the identified zones include the heat-affected zone (HAZ), which experiences thermal exposure without mechanical deformation; the thermo-mechanical affected zone (TMAZ) which is partially deformed, located between the HAZ and the extruded rod; and the stir zone (SZ), primarily found within the extruded rod. Each zone exhibits distinct microstructures due to the varying influence of mechanical deformation and thermal exposure imposed by different rotational speeds. In Fig. 7, refined grains are

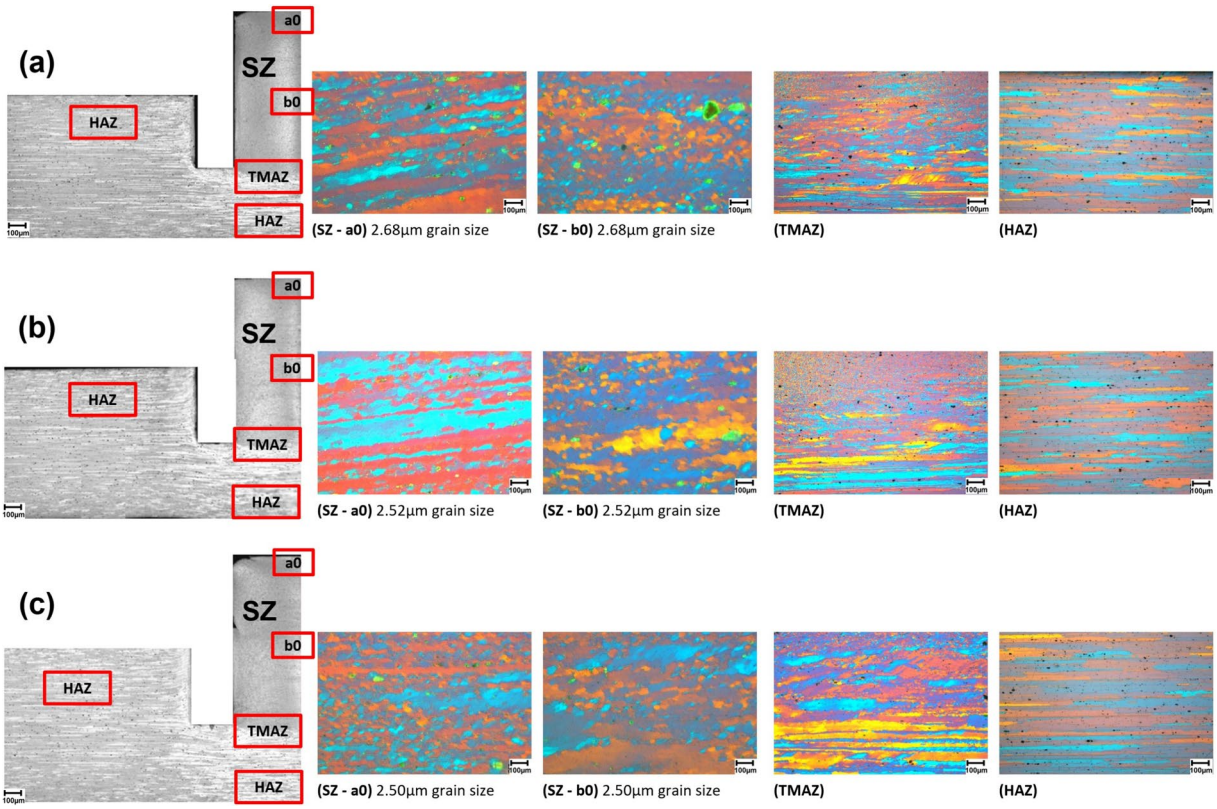

Fig. 7 Grain morphology at different microstructural zones and rotational speeds: (**a**) 1000 rpm, (**b**) 1200 rpm, and (**c**) 1400 rpm

observed in the SZ for all rotational speeds, with an average grain size of approximately 2.56 µm. The grain morphology and the grain sizes show a significant refinement, which is attributed to the occurrence of DRX. The occurrence of DRX in AA7075 is likely dominated by continuous dynamic DRX due to their high stacking fault energy and low shear modulus [33]. Continuous dynamic DRX is characterized by the transformation of low-angle grain boundaries (LAGBs) into high-angle grain boundaries (HAGBs), leading to the breakup of large grains into small grains of approximately 2-3 µm as reported in literature [2]. The TMAZ reveals mostly elongated and partially deformed grains, especially in the region close to the SZ. In the TMAZ, the thermal exposure is moderate, but not sufficient to induce DRX. The HAZ retains the elongated and undeformed grain structure of the BM.

Next to the material deformation, the local temperature evolution strongly influences the microstructure evolution in AA7075, in particular the precipitation kinetics. Therefore, Fig. 8 shows the simulated temperature distribution across the workpiece cross-section after the plunging phase, alongside corresponding experimental micrographs. Increasing the rotational speed from 1000 to 1400 rpm raises the maximum and uniform temperature in the SZ from 423°C to 480°C. At local temperatures approximately above 400 °C, as observed in the SZ, DRX becomes dominant, with an enhanced transformation of LAGBs into HAGBs, thereby reducing LAGBs length, as reported in literature [34]. The TMAZ serves as a transition zone, where the temperature gradually decreases from the SZ towards the HAZ.

In Fig. 9(a) at 1000 rpm, the maximum hardness observed in the SZ is 196 HV, with an average of 175 ± 5 HV (±2.8%). The hardness map reveals a relatively homogeneous distribution of high hardness values across the SZ. In the TMAZ, the hardness decreases progressively toward the HAZ, reflecting a decrease in the precipitate

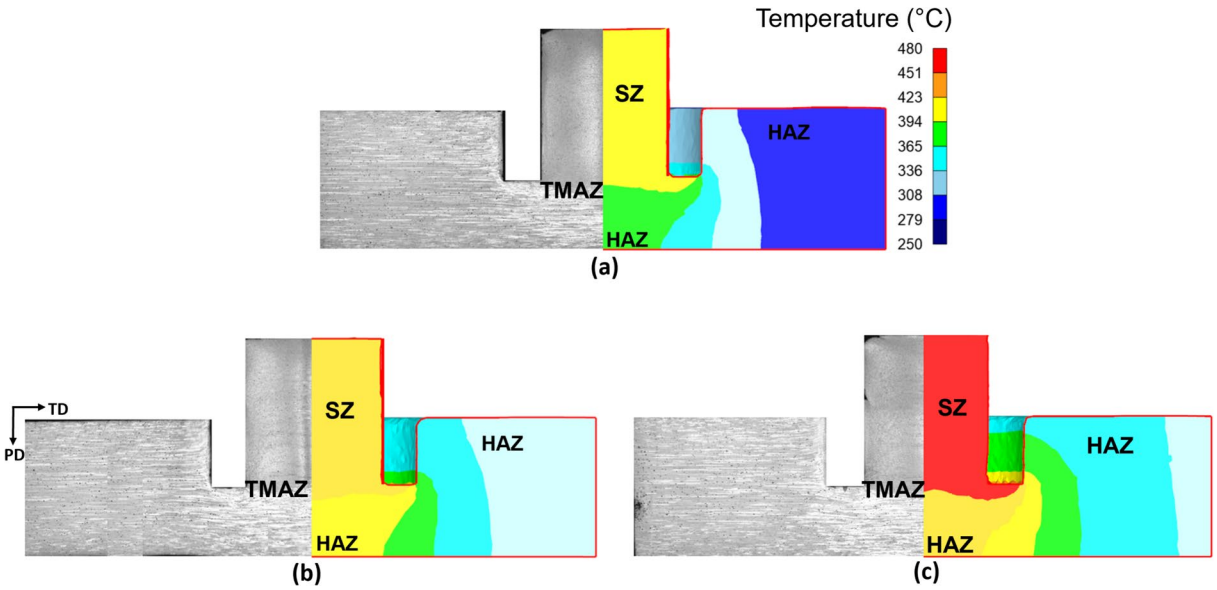

Fig. 8 Micrographs and spatial temperature distributions for different rotational speeds: (**a**) 1000 rpm, (**b**) 1200 rpm, and (**c**)1400 rpm

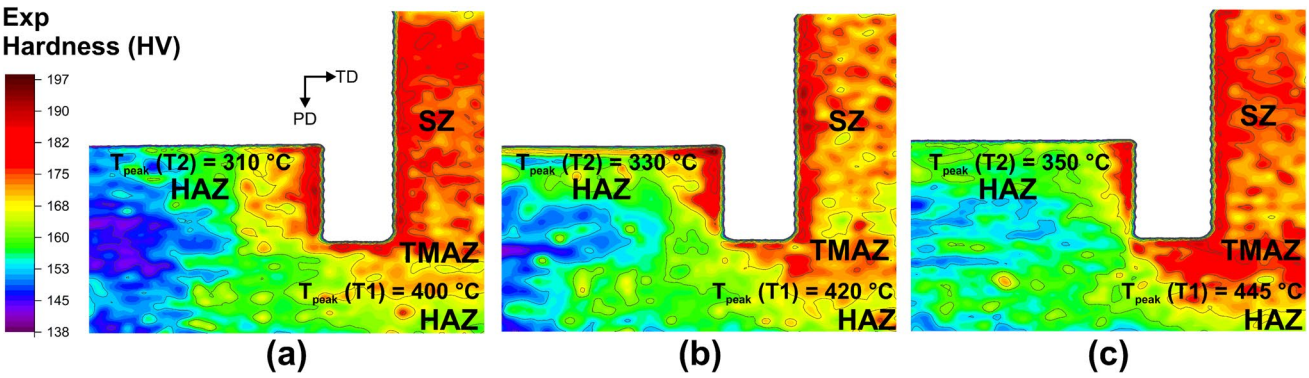

Fig. 9 Spatial distribution of experimental hardness in the workpiece at different rotational speeds: (**a**) 1000 rpm, (**b**) 1200 rpm, and (**c**) 1400 rpm

strengthening mechanism in this region in relation to the SZ. The HAZ, where the maximum temperature is 310° C, exhibits a further decrease in hardness, from 168 HV to 160 HV, as it approaches the outer edge in this region. In Fig. 9(b) at 1200 rpm, the hardness peak in the SZ is determined as 196 HV, with an average of 172 ± 5 HV (±3.1%), comparable to that at 1000 rpm (Fig. 9(a)). However, unlike the relatively uniform distribution at 1000 rpm, the hardness within the SZ becomes less homogeneous. A decrease in hardness, from 176 HV at the periphery to 171 HV at the core. The lower hardness at the core can be attributed to coarse precipitates located at the HAGBs during the cooling stage as documented in literature [35, 36]. However, the hardness trends in TMAZ and HAZ remain broadly like those observed at 1000 rpm. In Fig. 9(c) at 1400 rpm, the SZ exhibits an average hardness of 174 ± 4 HV (±2.4%) and a more homogeneous hardness distribution, similar to the trend at 1000 rpm rather than the heterogeneous profile at 1200 rpm. The peak hardness observed in the region is determined as 189 HV. Moreover, the higher hardness values observed in the SZ spatially extend toward the TMAZ at 1400 rpm, compared to 1000 rpm and 1200 rpm.

Overall, a significant increase in local hardness in the SZ to around 25% in relation to the base material is observed in all cases. Although the hardness maps show slightly distinct trends in the SZ, the analysis of the local average hardness and the corresponding standard deviation for each RS (around 3% in all cases) indicates that these variations are not statistically significant and can be interpreted as intrinsic to the experiments. Since the SZ predominantly defines the extruded rod, the following section focuses on analyzing material flow within this region.

Constrained and helical material flow behavior due to deformation parameters in CFP

Investigating the evolution of material flow patterns and characteristics in the SZ assists in establishing a correlation between continuous shear deformation, microstructure evolution, and the consequent development of material flow. The material flow presented is deduced at the symmetry axis of the extruded rod, where the major shear deformations occur during the process. Figure 10(a) illustrates the evolution of a helical material flow within the SZ

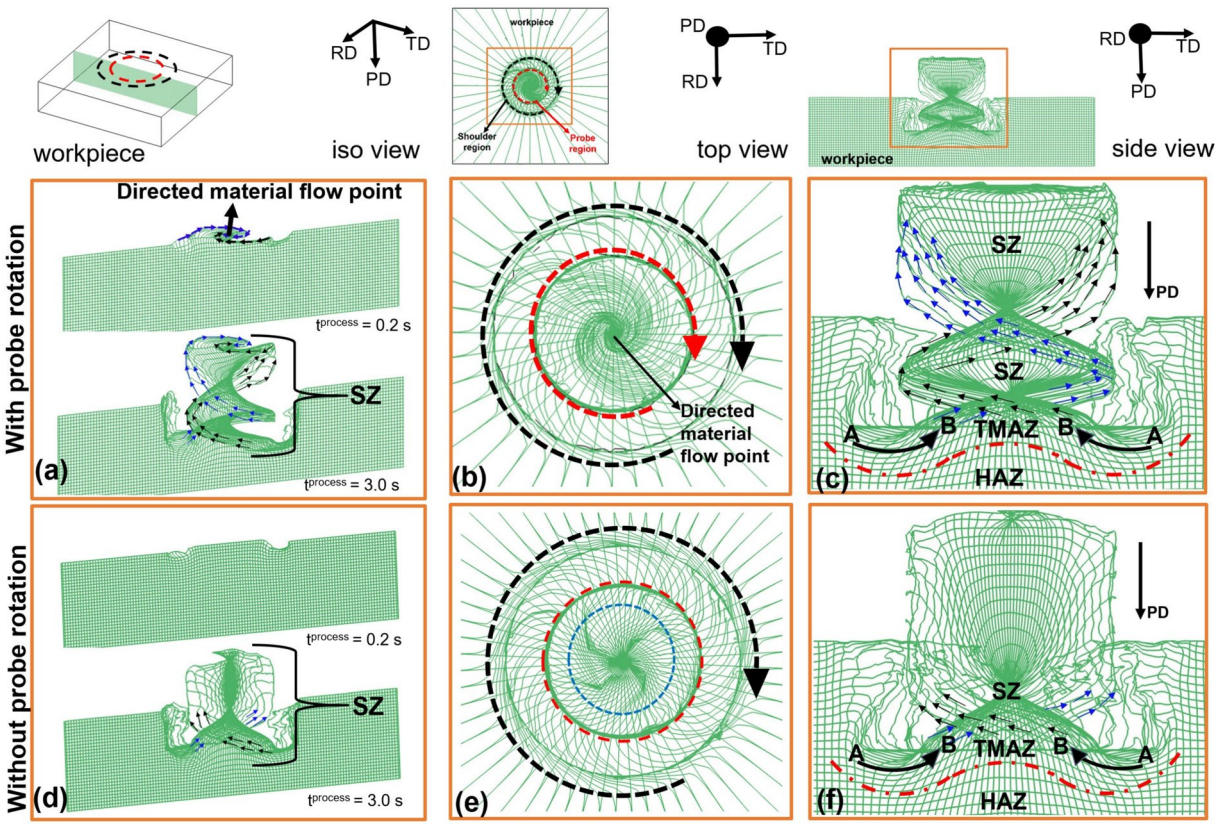

Fig. 10 Simulated material flow path at 1400 rpm: (**a**) evolution of helical flow pattern in iso view, (**b**) 2D spiral flow pattern in radial direction (top view) at $t^{process}$ = 3.0 s, (**c**) flow pattern in the plunge direction (side view) at $t^{process}$ = 3.0 s, (**d**) evolution of flow pattern in iso view, (**e**) flow pattern in radial direction (top view) at $t^{process}$ = 3.0 s, and (**f**) flow pattern in plunge direction at $t^{process}$ = 3.0 s. The blue dash circle in (**e**) is at 1.8 mm and a transition region in the extrudate. The red dash lines in (**c**) and (**f**) are transition regions between TMAZ and HAZ

at 1400 rpm. This rotational speed is used as an example, as other speeds exhibit a similar trend. At 0.2 s, the flow pattern emerges from the interaction of the rotating shoulder and probe, which are in contact with the material. As the processing time progresses to 3.0 s, a more defined cylindrical helical flow develops, driven by shear deformation and upward material movement, primarily induced by the radial movement of the shoulder and probe as well as the vertical movement of the shoulder. This combined flow pattern reflects the material movement within the SZ during processing. At the region under the shoulder, a significant radial material flow pattern is observed, which symmetrically aligns with the tool center point. At the extrudate section, i.e. region under the probe, the material flow forms a 2D spiral flow pattern due to the completely plasticized material compared to the position under the shoulder. Additionally, the rotation of the probe, which is constraining the material, leads to a directed material flow at the center of the tool, see Fig. 10(b).

Figure 10(c) illustrates the material flow from point A (under the shoulder) towards point B, leading to the formation of the SZ located within the shoulder cavity. As the material flows into the shoulder cavity, the constraints imposed by the surrounding tool surfaces promote intense shearing, leading to the formation of a helical flow pattern within the cavity. The probe, in particular, imposes an additional constraint that contributes to the compressive component of the overall stress state arising from the thermo-mechanical conditions of the process. This enhances the ability of the applied rotation to propagate shear deformation throughout the extrudate. This mechanism assists in the complete breaking of long parent grains and stirring material within the SZ, leading to the complex flow path depicted see Fig. 10(c). Furthermore, this flow signifies the breakup of non-uniformities in the material structure, such as secondary phases and volumetric defects [14], leading to a more homogeneous microstructure.

To understand the contribution of probe rotation to constrained material flow, the CFP process is also conducted without probe rotation. Figure 10(d) shows that, in this case, both the initial radial directed flow pattern and the helical flow are not prominently present under the probe or within the shoulder cavity. This can be attributed to less shear deformation occurring at the core of the extrudate due to constrained flow behaviour in the absence of probe rotation. The radial material flow beneath the extrudate's radial cross-section is significantly influenced, as deformation primarily occurred in the outer region due to shoulder rotation, while the inner radius within the extrudate remained only partially deformed and consolidated, see Fig. 10(e). This indicates a transition region between the shoulder and probe-constrained deformation during processing. The findings suggest that solely relying on shoulder rotation might be insufficient to achieve complete DRX in the SZ.

Figure 10(f) illustrates the material flow into the shoulder cavity for constrained flow behaviour without probe rotation. The helix-like flow pattern present between the TMAZ and SZ (at the base of the rod), is similar to the flow pattern observed when both the shoulder and probe are rotating. This suggests the dominant contribution of the shoulder-induced deformation and flow in this region of the extrudate. Along the plunge direction, the helix-like character of the material flow is progressively less pronounced. To validate the contribution of the tools, the radial dependency of the flow is further analyzed without the presence of the probe.

In order to assess the contribution of the probe to the CFP and allow a direct comparison with other friction-extrusion processes, a modified CFP simulation is established, excluding the probe in the assembly. Figure 11 shows the comparison of the simulated shoulder-induced radial deformation and material flow for CFP and modified CFP, validated against the experimental microstructure. Cross-sections of the extrudate along the radial direction are analyzed for each of the cases previously discussed, i.e. CFP, which features the probe as an additional rotating tool to constrain the material flow during the extrusion, and its counterpart without probe, which mimics the FE process. In CFP with probe rotation, the micrograph presented in Fig. 11(a) reveals a dispersion of the tracer material in a clear 2D spiral flow pattern. This observation matches the predictions established in Fig. 11(b) with the yellow arrow in Fig. 11(c) showing comparable directed flow lines. For the CFP experiment without the probe (see Fig. 11(d)) and the corresponding simulation result in Fig. 11(e), two distinct regions can be identified based on the material's deformation history. At the periphery of the extrudate, the volume of material in close contact with the shoulder rotating surface is stirred in layers, and dynamically recrystallized, as visualized in more detail in Fig. 11(f). At the center of the extrudate, it can be seen that the material microstructure is very similar to the as-rolled microstructure of the base material, with large and elongated grains, indicating that the mechanical stresses submitted to this volume of material are not sufficient to induce a material flow along the radial direction, preventing the material from being stirred. Once again, the observations of the microstructures align with the predictions from the model, with the two identified shoulder-induced and probe-induced deformation regions.

The above study focuses on the numerical prediction of thermal evolution and material flow during CFP of AA7075 under a limited range of processing conditions. While the model successfully captures temperature fields and flow patterns validated against experimental measurements,

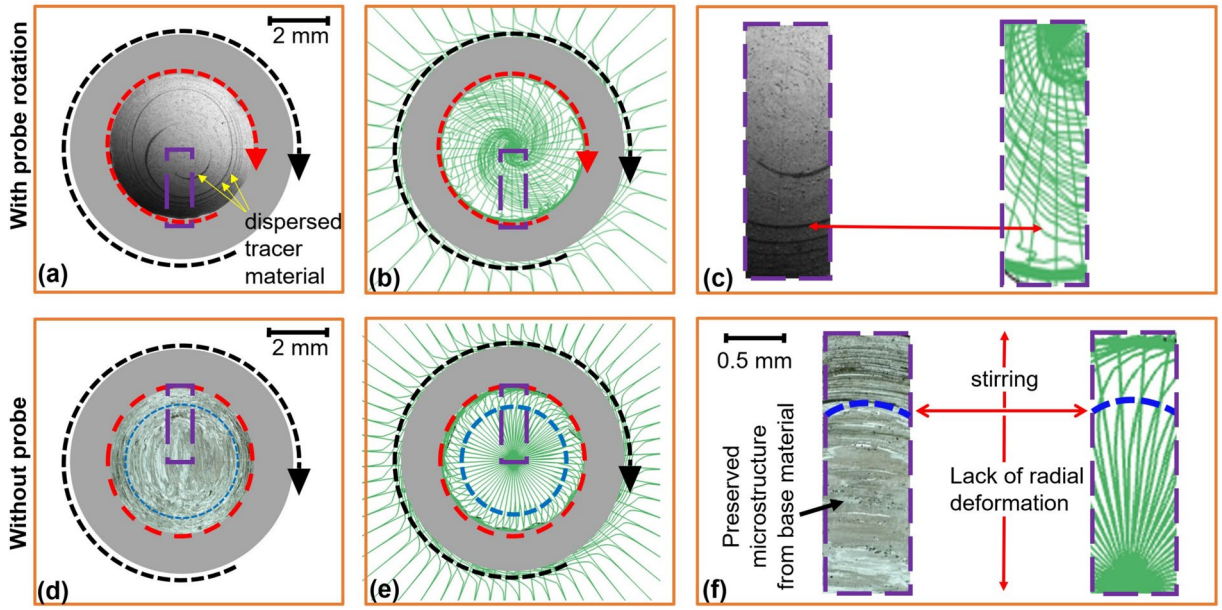

Fig. 11 Comparison between simulation and experimental results obtained for the extrudate for the validation of the material flow for the case of conventional CFP with the probe (**a**-**b**), with the flow line shown in detail in (**c**). Results without the probe (**d**-**e**), with the regions highlighted in purple, are presented in higher magnification in (**f**)

microstructural evolution and hardness variations are interpreted indirectly based on established physical mechanisms rather than being explicitly modeled.

Conclusion

This study implemented an FEM model for CFP to capture the thermo-mechanical response and material flow behavior during aluminum alloy processing. The main conclusions are summarized as follows:

- The deformation history reveals that both the shoulder and probe contribute to shear deformation. While the shoulder primarily concentrating deformation near the periphery, the probe imposes a constraint in the material, generating a compressive component in the stress state within the core of the extrudate that enhances shear deformation.
- Higher rotational speeds increase temperatures, promoting material softening and reducing the forces required to extrude the material. However, shoulder forces are still consistently higher than probe forces because the shoulder plunges directly into the workpiece.
- The SZ consistently exhibited a refined microstructural region with a similar length in the rod, and the TMAZ revealed partially deformed grains across all rotational speeds. These microstructural characteristics are accurately reproduced in the FEM simulation through the corresponding spatial temperature distribution.
- In the SZ, a significant increase in hardness of 25% relative to the base material is observed for all RS, primarily due to the higher heat input, which accelerates precipitate kinetics.
- The addition of probe rotation enhances radial flow line and promotes the formation of helical flow patterns, thereby enabling microstructural tailoring of the extrudate. In the case of no rotation, the radial flow at the core is constrained, which impedes complete core stirring and prevents the formation of complete helical flow.
- In the absence of a probe, the primary deformation induced solely by the shoulder is insufficient to induce substantial material flow, leading to less distinct flow features in the extrudate core.

Author Contributions G.D -Conceptualization, Data curation, Formal analysis, Investigation, Methodology, Writing-original draft, Validation, Visualization, Writing – review and editing. C.C - Investigation, Data curation, Writing – review and editing. R.C - Supervision, Investigation, Writing B.K - Funding acquisition, Resources, Supervision, Conceptualization, Writing – review and editing

Funding Open Access funding enabled and organized by Projekt DEAL.

Data Availability The data related to this research is available online (https://doi.org/10.5281/zenodo.18348048).

Declarations

Competing interests The authors declare no competing interests.

References

1. Haghshenas M, Gerlich A (2018) Joining of automotive sheet materials by friction-based welding methods: A review. Eng Sci Technol Int J 21(1):130–148. https://doi.org/10.1016/j.jestch.2018.02.008
2. Baghdadchi A, Patel V, Li W, Yang X, Andersson J (2023) Ductilization and grain refinement of AA7075-T651 alloy via stationary shoulder friction stir processing. J Market Res 27:5360–5367. https://doi.org/10.1016/j.jmrt.2023.11.041
3. Shen Z, Ding Y, Gerlich AP (2020) Advances in friction stir spot welding. Crit Rev Solid State Mater Sci 45(6):457–534. https://doi.org/10.1080/10408436.2019.1671799
4. Chen G, Zhang S, Zhu Y, Yang C, Shi Qy (2019) Thermomechanical analysis of friction stir welding: A review on recent advances. Acta Metallurgica Sinica (English Letters). https://doi.org/10.1007/s40195-019-00942-y
5. Tang J, Wang J, Teng J, Wang G, Fu D, Zhang H, Jiang F (2021) Effect of zn content on the dynamic softening of Al–Zn–Mg–Cu alloys during hot compression deformation. Vacuum 184:109941. https://doi.org/10.1016/j.vacuum.2020.109941
6. Zhang H, Li L, Yuan D, Peng D (2007) Hot deformation behavior of the new Al-Mg-Si-Cu aluminum alloy during compression at elevated temperatures. Mater Charact 58(2):168–173. https://doi.org/10.1016/j.matchar.2006.04.012
7. Cao F, Zheng J, Jiang Y, Chen B, Wang Y, Hu T (2019) Experimental and DFT characterization of η' nano-phase and its interfaces in Al-Zn-Mg-Cu alloys. Acta Mater 164:207–219. https://doi.org/10.1016/j.actamat.2018.10.045
8. Liu D, Xiong B, Bian F, Li Z, Li X, Zhang Y, Wang Q, Xie G, Wang F, Liu H (2015) Quantitative study of nanoscale precipitates in Al–Zn–Mg–Cu alloys with different chemical compositions. Mater Sci Eng, A 639:245–251. https://doi.org/10.1016/j.msea.2015.04.104
9. Zang R, Ding L, Ehlers FJ, Jia Z, Xu S, Li Y, Cao L (2023) The influence of Cu content and Mg/Si ratio on the strength and formability in Al-Mg-Si-Cu alloys. Mater Charact 205:113355. https://doi.org/10.1016/j.matchar.2023.113355
10. Zhang S, Kontsevoi OY, Freeman AJ, Olson GB (2011) First principles investigation of zinc-induced embrittlement in an aluminum grain boundary. Acta Mater 59(15):6155–6167. https://doi.org/10.1016/j.actamat.2011.06.028
11. Xiao G, Jiang J, Liu Y, Wang Y, Guo B (2019) Recrystallization and microstructure evolution of hot extruded 7075 aluminum alloy during semi-solid isothermal treatment. Mater Charact 156:109874. https://doi.org/10.1016/j.matchar.2019.109874
12. Li Z, Chen L, Tang J, Sun W, Zhao G, Zhang C (2021) Improving mechanical anisotropy and corrosion resistance of extruded AA7075 alloy by warm cross rolling and annealing. J Alloy Compd 863:158725. https://doi.org/10.1016/j.jallcom.2021.158725
13. Elibol C, Sagir K, Dogan M (2024) Effect of equal-channel angular pressing on microstructure, aging kinetics and impact behavior in a 7075 aluminum alloy. Mater Today Commun 39:108931. https://doi.org/10.1016/j.mtcomm.2024.108931
14. de Castro CC, Shen J, dos Santos JF, Klusemann B (2023) Microstructural development of as-cast AM50 during constrained friction processing: Grain refinement and influence of process parameters. J Mater Process Technol 318:0–118018. https://doi.org/10.1016/j.jmatprotec.2023.118018
15. Schilling C, dos Santos J (2004) Method and device for joining at least two adjoining work pieces by friction welding. U.S. Patent pp 6,722–556
16. Baffari D, Buffa G, Fratini L (2017) A numerical model for wire integrity prediction in friction stir extrusion of magnesium alloys. J Mater Process Technol 247:1–10. https://doi.org/10.1016/j.jmatprotec.2017.04.007
17. Chen T, Fu B, Shen J, Suhuddin UF, Wiese B, Huang Y, Wang M, dos Santos JF, Bergmann JP, Klusemann B (2023) Application of novel constrained friction processing method to produce fine grained biomedical Mg-Zn-Ca alloy. J Magnes Alloys. https://doi.org/10.1016/j.jma.2023.10.007
18. de Castro CC, Neves AM, Klusemann B (2024) Effect of thermomechanical conditions during constrained friction processing on the particle refinement of AM50 Mg-alloy phases. J Magnes Alloys 12(6):2298–2311. https://doi.org/10.1016/j.jma.2024.04.002
19. Zhang H, Zhao X, Deng X, Sutton M, Reynolds A, McNeill S, Ke X (2014) Investigation of material flow during friction extrusion process. Int J Mech Sci 85:130–141. https://doi.org/10.1016/j.ijmecsci.2014.05.011
20. Li L, Reza-E-Rabby M, Overman N, Wang T, Whalen S, Grant G, Mathaudhu S, Soulami A (2022) Analysis of contact conditions and microstructure evolution in shear assisted processing and extrusion using smoothed particle hydrodynamics method. Mater Des 221:111010. https://doi.org/10.1016/j.matdes.2022.111010
21. Baffari D, Buffa G, Campanella D, Fratini L, Reynolds AP (2017) Process mechanics in friction stir extrusion of magnesium alloys chips through experiments and numerical simulation. J Manuf Process 29:41–49. https://doi.org/10.1016/j.jmapro.2017.07.010
22. Alewi D, Murdoch H, Magagnosc D, Lemmen K, Karaca H, Rottmann P (2024) Depth-dependent microstructure and mechanical properties of hot rolled AA7075. Mater Sci Eng, A 892:146056. https://doi.org/10.1016/j.msea.2023.146056
23. Bodunrin MO (2020) Flow stress prediction using hyperbolic-sine arrhenius constants optimised by simple generalised reduced gradient refinement. J Market Res 9(2):2376–2386. https://doi.org/10.1016/j.jmrt.2019.12.070
24. Asadi P, Mahdavinejad R, Tutunchilar S (2011) Simulation and experimental investigation of FSP of AZ91 magnesium alloy. Mater Sci Eng, A 528(21):6469–6477. https://doi.org/10.1016/j.msea.2011.05.035
25. Garg A, Bhattacharya A (2017) On lap shear strength of friction stir spot welded AA6061 alloy. J Manuf Process 26:203–215. https://doi.org/10.1016/j.jmapro.2017.02.019
26. Jain R, Pal S, Singh S (2018) Thermomechanical Simulation of Friction Stir Welding Process Using Lagrangian Method, pp 103–146. https://doi.org/10.1007/978-981-10-8518-5_4
27. Jain R, Pal SK, Singh SB (2016) A study on the variation of forces and temperature in a friction stir welding process: A finite element approach. J Manuf Process 23:278–286. https://doi.org/10.1016/j.jmapro.2016.04.008
28. Wang L, Yang H (2012) Friction in aluminium extrusion—part 2: A review of friction models for aluminium extrusion. Tribol Int 56:99–106. https://doi.org/10.1016/j.triboint.2012.06.006

29. Rokni M, Zarei-Hanzaki A, Roostaei AA, Abolhasani A (2011) Constitutive base analysis of a 7075 aluminum alloy during hot compression testing. Mater Des 32(10):4955–4960. https://doi.org/10.1016/j.matdes.2011.05.040
30. Trimble D, O'Donnell G (2015) Constitutive modelling for elevated temperature flow behaviour of AA7075. Mater Des 76:150–168. https://doi.org/10.1016/j.matdes.2015.03.062
31. Buffa G, Hua J, Shivpuri R, Fratini L (2006) A continuum based FEM model for friction stir welding—model development. Mater Sci Eng, A 419(1):389–396. https://doi.org/10.1016/j.msea.2005.09.040
32. Dalai B, Moretti MA, Åkerström P, Arvieu C, Jacquin D, Lindgren LE (2021) Mechanical behavior and microstructure evolution during deformation of AA7075-T651. Mater Sci Eng, A 822:141615. https://doi.org/10.1016/j.msea.2021.141615
33. Chen S, Li D, Zhang S, Han H, Lee H, Lee M (2020) Modelling continuous dynamic recrystallization of aluminum alloys based on the polycrystal plasticity approach. Int J Plast 131:102710. https://doi.org/10.1016/j.ijplas.2020.102710
34. Jiang S, Lv J, Shi Z, Lin J (2024) A study of dynamic recovery and recrystallisation mechanisms in aluminium alloy AA7050 at different thermomechanical processing conditions. Mater Sci Eng, A 914:147117. https://doi.org/10.1016/j.msea.2024.147117
35. Lezaack MB, Simar A (2021) Avoiding abnormal grain growth in thick 7xxx aluminium alloy friction stir welds during T6 post heat treatments. Mater Sci Eng, A 807:140901. https://doi.org/10.1016/j.msea.2021.140901
36. Jadot M, Li J, Gautier R, Xie J, Lezaack MB, Sapanathan T, Rachik M, Simar A (2025) Analysis of grain structure, precipitation and hardness heterogeneities, supported by a thermal model, for an aluminium alloy 7075 deposited by solid-state multi-layer friction surfacing. J Mater Process Technol 335:118661. https://doi.org/10.1016/j.jmatprotec.2024.118661